

Advance Publication Cover Page



Insight into a structural demand for cold crystallization of small molecule. A case study for Schiff base compounds that exhibit prototropic tautomerization

Katsunori Iwase,* Yasuhiro Toyama, Isao Yoshikawa, Yasuhisa Yamamura,
Kazuya Saito, and Hirohiko Houjou*

Advance Publication on the web February 22, 2018

doi:10.1246/bcsj.20170386

© 2018 The Chemical Society of Japan

Advance Publication is a service for online publication of manuscripts prior to releasing fully edited, printed versions. Entire manuscripts and a portion of the graphical abstract can be released on the web as soon as the submission is accepted. Note that the Chemical Society of Japan bears no responsibility for issues resulting from the use of information taken from unedited, Advance Publication manuscripts.

Insight into a structural demand for cold crystallization of small molecule. A case study for Schiff base compounds that exhibit prototropic tautomerization

Katsunori Iwase,*¹ Yasuhiro Toyama,¹ Isao Yoshikawa,² Yasuhisa Yamamura,³ Kazuya Saito³ and Hirohiko Houjou*²

¹DENSO CORPORATION, 500-1 Minamiyama, Komenoki-cho, Nisshin, Aichi 470-0111, JAPAN

²Institute of Industrial Science, The University of Tokyo, 4-6-1 Komaba, Meguro-ku, Tokyo 153-8505, JAPAN

³Department of Chemistry, Faculty of Pure and Applied Sciences, University of Tsukuba, Tsukuba, Ibaraki 305-8571, JAPAN

E-mail: katsunori_iwase@denso.co.jp



Katsunori Iwase

Katsunori Iwase received Ph.D. from University of Tsukuba in 2015. He works for DENSO CORPORATION and engaged in functional material research at Advanced Research and Innovation Center.



Hirohiko Houjou

Hirohiko Houjou received his Ph.D. degree from Tokyo Institute of Technology in 1998. He worked for National Institute of Advanced Interdisciplinary Research, National Institute of Advanced Industrial Science and Technology, and moved to the present affiliation in 2003. Specialized in physical organic chemistry, he studies the properties of various molecular assemblies using solid-state spectroscopy and quantum chemical calculations.

Abstract

To elucidate the relationship between prototropic tautomerism and the cold crystallization phenomenon, *o*-hydroxy aryl Schiff base compounds derived from three different toluidine isomers were examined. Comparing their thermal behavior, we confirmed that cold crystallization occurred to give a different crystalline phase compared to the initial state. To elucidate the mechanisms of the cold crystallization of the materials, their thermal, structural, and energetic properties were investigated. The DFT calculation of the molecules in their OH- and NH-forms suggested that the NH-form has higher molecular flexibility, which may prevent normal crystallization upon cooling, compared to the OH-form. Spectroscopic analyses implied that the molecules are present as a mixture of the OH- and NH-forms, and that they efficiently crystallize when a preferable OH / NH ratio is achieved. For this molecular system, we concluded that the equilibrium between NH- and OH-forms controls the supercooling of the liquid as well as nucleation and crystal growth.

1. Introduction

Primary energy sources like petroleum and natural gas are ultimately discharged in the form of product gases and waste heat after consumption in automobiles, factories, and households. The effective use of this waste heat can contribute to improving the energy efficiency of mechanical and electric systems, and thus reducing their CO₂ emissions. To achieve this goal, technologies for heat storage,¹⁾ heat exchange,²⁾ heat extraction,³⁾ and related processes must be improved. Among these processes, especially for automobiles, heat storage is highly desired because of the importance of eliminating the lag time between the initial demand and eventual supply of heat. The ideal behavior of heat storage materials would include 1) storing heat when and where surplus heat is generated, 2)

maintaining the heat storage state at room temperature, and 3) releasing heat when and where it is required.

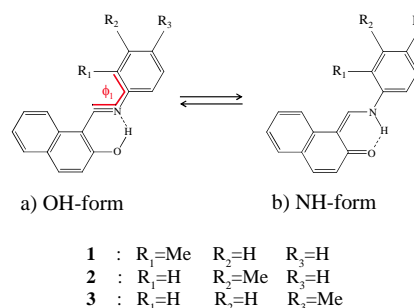


Figure 1. Molecular structures of the Schiff base-compounds studied.

Cold crystallization is an interesting phenomenon because the crystallizing material shows exothermic anomalies during the heating process. As a prerequisite, cold crystallization materials should show supercooling during the cooling process to maintain a molten or glass state, so that the crystallization can occur in the subsequent heating process. Since these prerequisites match the thermal behavior required from heat storage materials, cold crystallization materials are potentially applicable to heat storage. To date, there have been several reports of polymers⁴⁻⁶⁾, ionic liquids⁷⁾, organic matter⁸⁻¹¹⁾, and metal complexes¹²⁻¹⁶⁾ as cold crystallization materials. However, there are many aspects that remain unclear with respect to the mechanism of cold crystallization.

Recently, Iwase et al. reported that certain Schiff base complexes exhibit cold crystallization behavior, and attempted to elucidate their cold crystallization mechanism. They proposed two design guidelines for cold crystallization materials: 1) to introduce a flexible moiety in the molecule to

increase the degree of freedom of molecular motion^{17,18}), and 2) allow several isomers that are interconvertible to coexist in the liquid (molten) state to disturb the homogeneity of the system¹⁹. In accordance with these guidelines, Achira et al. reported that a two-component molecular system can also cause cold crystallization.²⁰

In the present study, we focused on 2-hydroxy-1-naphthaldehyde Schiff bases (**1**, **2** and **3**) of *o*-, *m*-, and *p*-toluidine, respectively. These compounds show prototropic tautomerism (Figure 1) by intramolecular proton transfer between the oxygen and nitrogen atoms, resulting in equilibrium between the keto-enamine (NH-form) and enol-imine form (OH form).^{21,22} The OH/NH-form ratio varies depending on molecular and crystal structures, temperature, and photo-irradiation²³. Consequently, these compounds follow the second guideline, and are potential candidates for cold crystallization. However, there have been no studies that have focused the effect of tautomerization on cold crystallization. The purpose of this study is to observe cold crystallization of the three Schiff base compounds and to elucidate their mechanisms from the viewpoint of structural chemistry.

2. Experimental

2.1 Synthesis. The Schiff base compounds **1–3** were prepared according to a reported procedure for condensation of salicylaldehyde and aniline.^{17–19} In a typical example, to a hot ethanol solution (50 mL) of 2-hydroxy-1-naphthaldehyde (3.44 g, 20.0 mmol) was added *p*-toluidine (2.14 g, 20.0 mmol). The mixture was stirred at 70°C for 1 h, and then concentrated to about 40 mL with vacuum evaporator, to afford yellow crystalline precipitate. The product was collected by filtration, washed with ethanol, and dried under reduced pressure. All the chemicals and solvents were purchased from Tokyo Chemical Industry and used without further purification.

The products were characterized by IR spectroscopy using a JEOL FT/IR-420, elemental analysis (CHN) using a Fusion Instruments EA1108, ¹H and ¹³C NMR spectroscopy using a JEOL ECS-400 (400 MHz for ¹H). As for the compounds **1–3**, the resonance signals were successfully assigned by assuming their NH-form shown in Figure 1.²⁴ The melting points were determined as the onset temperature on the first heating run of DSC.

1-(2-methylphenyl)iminomethylnaphthalene : **1**

Yellow crystals (yield 4.24 g, 81%); m.p. 118.7°C; IR(KBr) 1622 cm⁻¹ (ν_{C=N}); MS (FAB+) *m/z* 262.1 (calcd. for M+H⁺ 262.13); Analysis calcd. for C₁₈H₁₅NO: C, 82.73; H, 5.79; N, 5.36; found: C, 82.53; H, 5.79; N, 5.20; ¹H NMR (CDCl₃) δ = 2.49 (s, 3H), 7.08 (d (*J* = 8.7 Hz), 1H), 7.19–7.22 (mult, 1H), 7.30–7.35 (mult, 4H), 7.52 (dt (*J* = 7.8 Hz, 1.6 Hz), 1H), 7.71 (d (*J* = 7.8 Hz), 1H), 7.80 (d (*J* = 9.1 Hz), 1H), 8.10 (d (*J* = 9.1 Hz), 1H), 9.31 (d (*J* = 5.4 Hz), 1H), 15.76 (d (*J* = 4.9 Hz), 1H); ¹³C NMR (CDCl₃) δ = 18.2, 108.8, 117.1, 118.7, 122.7, 123.5, 126.5, 127.1, 127.3, 128.1, 129.4, 130.9, 131.1, 133.3, 137.0, 143.5, 153.7, 171.8.

1-(3-methylphenyl)iminomethylnaphthalene : **2**

Yellow crystals (4.43 g, 85%), m.p. 92.4°C, IR(KBr) 1625 cm⁻¹ (ν_{C=N}); MS (FAB+) *m/z* 262.1 (calcd. for M+H⁺ 262.13); Analysis calcd. for C₁₈H₁₅NO: C, 82.73; H, 5.79; N, 5.36; found: C, 82.48; H, 5.77; N, 5.22; ¹H NMR (CDCl₃) δ = 2.43 (s, 3H), 7.05 (d (*J* = 9.7 Hz), 1H), 7.10 (d (*J* = 7.5 Hz), 1H), 7.15–7.17 (mult, 2H), 7.30–7.36 (mult, 2H), 7.50 (dt (*J* = 7.6 Hz, 1.6 Hz), 1H), 7.69 (d (*J* = 7.5 Hz), 1H), 7.77 (d (*J* = 9.7 Hz), 1H), 8.07 (d (*J* = 8.6 Hz), 1H), 9.27 (d (*J* = 5.4 Hz), 1H), 15.53 (d (*J* = 4.8 Hz), 1H); ¹³C NMR (CDCl₃) δ = 21.5, 108.6, 117.1, 118.7, 120.7, 122.9, 123.5, 127.1, 127.3, 128.1, 129.4, 129.5, 133.4, 137.0, 139.7, 144.4, 153.7, 171.9.

1-(4-methylphenyl)iminomethylnaphthalene : **3**

Yellow crystals (4.70 g, 90%), m.p. 137.6°C, IR(KBr) 1622 cm⁻¹ (ν_{C=N}); MS (FAB+) *m/z* 262.1 (calcd. for M+H⁺ 262.13); Analysis calcd. for C₁₈H₁₅NO: C, 82.73; H, 5.79; N, 5.36; found: C, 82.57; H, 5.80; N, 5.20; ¹H NMR (CDCl₃) δ = 2.40 (s, 3H), 7.06 (d (*J* = 9.8 Hz), 1H), 7.25–7.34 (mult, 5H), 7.51 (dt (*J* = 8.0 Hz, 1.3 Hz), 1H), 7.70 (d (*J* = 8.0 Hz), 1H), 7.78 (d (*J* = 8.8 Hz), 1H), 8.08 (d (*J* = 8.4 Hz), 1H), 9.31 (d (*J* = 4.9 Hz), 2H), 15.62 (d (*J* = 4.9 Hz), 1H); ¹³C NMR (CDCl₃) δ = 21.1, 108.6, 118.8, 120.0, 122.7, 123.4, 127.2, 128.0, 129.4, 130.3, 133.3, 136.5, 136.7, 142.2, 153.7, 171.1.

2.2 Crystallography. For single crystal structure analysis, **1-α** and **3-α** were picked up from the as-prepared sample, **2·MeOH** was recrystallized from methanol, **3-β** was recrystallized from ethanol. X-ray measurements on single crystals were carried out using diffractometers utilizing imaging plate with monochromated MoK α radiation (0.71075 Å). A Rigaku diffractometer (Tokyo, Japan) used was VariMax DW with Saturn. The structures were solved by the direct method (SHELXS2013 for **1-α**, **2·MeOH** and **3-β**, and il Milione for **3-α**)^{25,26} and refined by the full-matrix least-squares method on $|F|^2$. The non-hydrogen atoms were refined anisotropically. Hydrogen atoms were refined using the riding model. Absorption correction was applied using an empirical procedure. All calculations were performed using the CrystalStructure crystallographic software package except for refinement, which was performed using SHELXL2016 for **1-α**, **2·MeOH**, and **3-β**, or SHELXL97 for **3-α**.²⁵ Crystallographic data have been deposited with Cambridge Crystallographic Data Centre: Deposition numbers CCDC-1580131 to 1580134 to compounds **1**, **2**, and **3** (including polymorph). Copies of the data can be obtained free of charge via <http://www.ccdc.cam.ac.uk/conts/retrieving.html> (or from the Cambridge Crystallographic Data Centre, 12, Union Road, Cambridge, CB2 1EZ, UK; fax: +44 1223 336033; e-mail: deposit@ccdc.cam.ac.uk).

1-α: C₁₈H₁₅NO, *M_w* = 261.31, yellow needle, orthorhombic, space group *P*2₁2₁2₁, *a* = 7.337(4) Å, *b* = 12.402(6) Å, *c* = 14.367(7) Å, *V* = 1307.3(11) Å³, *Z* = 4, *D*_{calcd} = 1.328 g cm⁻³, *T* = 93(2) K, 10334 reflections collected, 2996 independent (*R*_{int} = 0.0673), GOF = 1.024, *R*₁ = 0.058, *wR*₂ = 0.120 for all reflections.

2·MeOH: C₁₈H₁₅NO·CH₃OH, *M_w* = 293.35, yellow needle, orthorhombic, space group *P*2₁2₁2₁, *a* = 5.823(3) Å, *b* = 15.804(6) Å, *c* = 16.545(7) Å, *V* = 1522.6(12) Å³, *Z* = 4, *D*_{calcd} = 1.280 g cm⁻³, *T* = 93(2) K, 10670 reflections collected, 2766 independent (*R*_{int} = 0.0881), GOF = 1.073, *R*₁ = 0.066, *wR*₂ = 0.116 for all reflections.

3-α: C₁₈H₁₅NO, *M_w* = 261.32, brown needle, orthorhombic, space group *P*na2₁, *a* = 19.797(10) Å, *b* = 13.846(7) Å, *c* = 4.877(2) Å, *V* = 1336.8(11) Å³, *Z* = 4, *D*_{calcd} = 1.298 g cm⁻³, *T* = 293 K, 2870 reflections collected, 1266 independent (*R*_{int} = 0.0315), GOF = 1.058, *R*₁ = 0.063, *wR*₂ = 0.165 for all reflections.

3-β: C₁₈H₁₅NO, *M_w* = 261.31, yellow needle, monoclinic, space group *P*2₁/*n*, *a* = 4.811(11) Å, *b* = 20.31(5) Å, *c* = 13.63(3) Å, β = 93.19(4)°, *V* = 1330(5) Å³, *Z* = 4, *D*_{calcd} = 1.305 g cm⁻³, *T* = 93.19(4) K, 7806 reflections collected, 2399 independent (*R*_{int} = 0.1867), GOF = 1.188, *R*₁ = 0.207, *wR*₂ = 0.543 for all reflections.

2.3 Thermal Analyses. Thermal analyses were conducted for **1–3** samples as prepared. The phase transition behavior of the complexes was investigated by differential scanning calorimetry (DSC) using a Mettler Toledo DSC-1. Open pans of aluminum were used under a nitrogen gas flow (50 mL

min⁻¹). The scanning rate was $\pm 15.0^\circ\text{C min}^{-1}$. Transition temperatures were determined as onset temperatures.

Simultaneous analyses of powder X-ray diffraction and DSC (XRD-DSC) were conducted for **1**–**3** samples as prepared, using a measurement system composed of a Rigaku SmartLab X-ray diffractometer and a Rigaku DSC. The sample was heated/cooled at a rate of $\pm 15^\circ\text{C min}^{-1}$ under N₂ atmosphere. During heating/cooling process, the XRD data were recorded for 2θ range of 5 – 50° at a scan speed of 45° min^{-1} . This means that one strip of XRD corresponds to a data during the temperature change of 15°C , unless otherwise noted. Monochromated CuK α radiation was used, and the voltage and current of the generator were 45 kV and 200 mA, respectively.

2.4 Solid-state UV-Vis spectroscopic analysis.

Solid-thin-film absorption spectra were measured for the **1**, **2** and **3** smeared onto glass slides at a sample thickness that yielded a maximum absorbance of about one. Each sample was placed on the stage of a conventional optical microscope equipped with a UV-transmitting objective lens and a portable

fiber optic spectrophotometer. Light from a xenon lamp was guided into the condenser lens through a quartz optical fiber and was focused on a selected $50\text{-}\mu\text{m}$ -diameter area of the sample.

Each spectrum, of which horizontal axis was converted to wavenumber (region of 19 – $27 \times 10^3\text{ cm}^{-1}$), was resolved to five gaussian components by a non-linear curve-fitting method (Marquardt method)²⁷⁾ coded into a home-made Wave-SPEC program.²⁸⁾ The initial values of the centers of the curves were set around 20 , 21 , 22 , 24 , $25 \times 10^3\text{ cm}^{-1}$. The examples of the resolution for **1**–**3** are given in the supplementary material (Figure S5–S7), and the parameters for the fitting were summarized in Table S1, S2, S3. After the peak resolution, the subarea summed over three curves at higher wavenumber, and that summed over the rest were calculated. The ratio of the former to the total peak area was defined as A_{SW} (area of short-wavelength component), which was tentatively adopted as a measure of the abundance of OH-form.

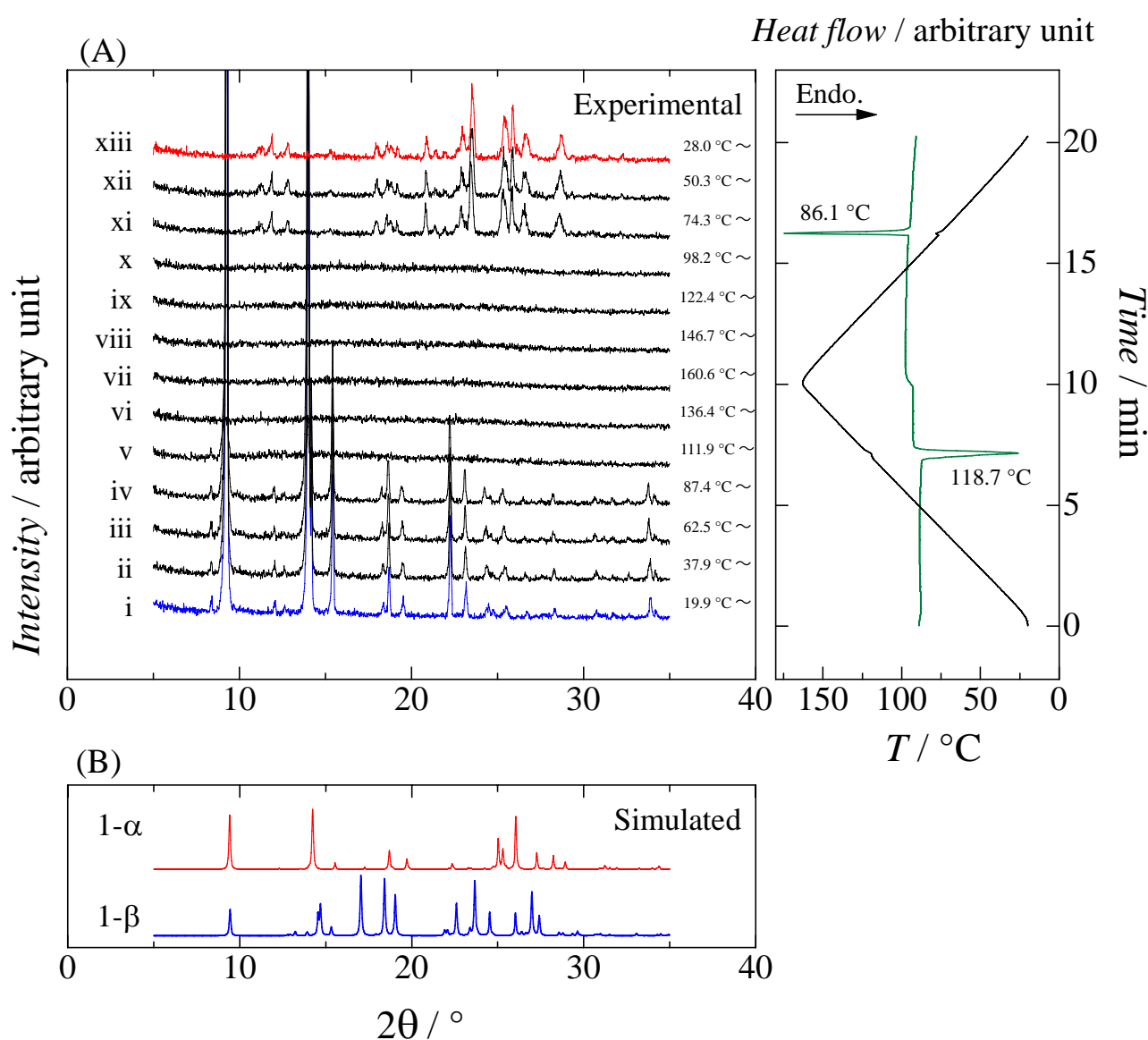


Figure 2. XRD-DSC results (A) of **1** obtained in first heating and subsequent cooling processes compared with simulated patterns (B) based on crystal structures (**1- α** and **1- β**) determined independently. Left, XRD ($5 \leq 2\theta / ^\circ \leq 35$); right, DSC (black line, temperature; green line, heat flow).

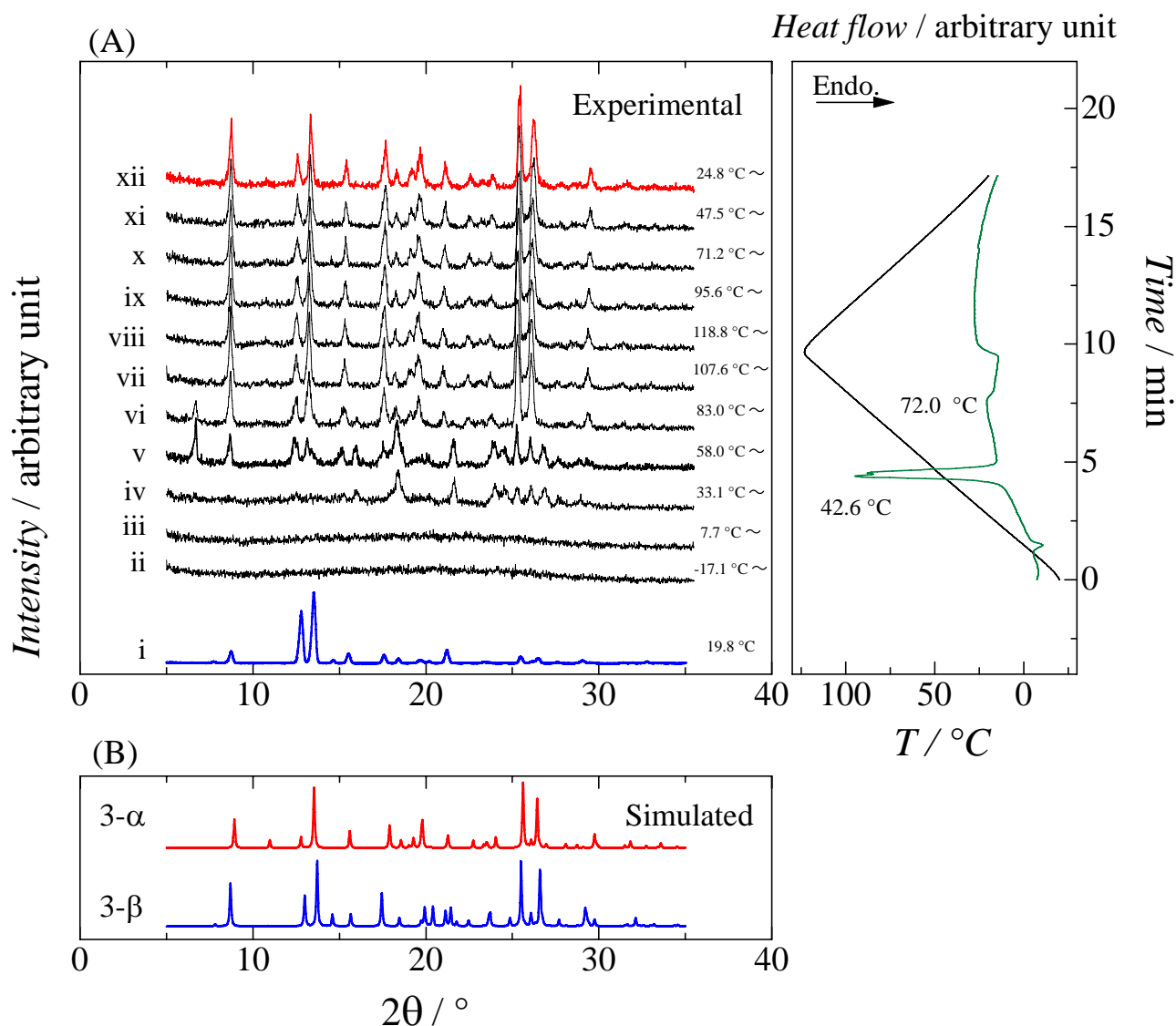


Figure 3. XRD-DSC results (A) of **3** obtained in second heating and subsequent cooling processes compared with simulated patterns (B) based on crystal structures (**3- α** and **3- β**) determined independently. Left, XRD ($5 \leq 2\theta / ^\circ \leq 35$); right, DSC (black line, temperature; green line, heat flow).

3. Results

3.1 Crystal Structures of 1 – 3. The Schiff base compounds **1–3** were readily obtained by simple condensation reaction in an ethanol solution. Although these compounds have been widely used for various metal complexes, we could not find any comprehensive analytical data of their structure and related properties in the literature. Also, there are surprisingly few reports on the crystal structures of **1–3** as free bases. As for **1**, two polymorphs were independently reported, CCDC116159²⁹⁾ (SIPFEC) and 998118³⁰⁾ (SIPFEC01). According to those reports, the former adopts the OH-form and melts at 128 °C, while the latter was assigned to the zwitterionic NH-form (no data for its melting point). In the present study, we found that product **1** (m.p. 118 °C) was crystallized in a form identical to the previously reported NH-form, and hereafter this phase is termed **1- α** . We tentatively call another phase **1- β** ,²⁹⁾ although we were not able to identify this type of crystal (Figure 2). As for **2**, we were not able to obtain a single crystal of good quality, without inclusion of solvent molecules. As prepared, compound **2** was a powdery microcrystalline solid that melts at 94 °C, which we call **2- α** . Recrystallization of **2- α** with methanol afforded a

pseudopolymorph including 1 eq. of a methanol molecule, which are labeled as **2·MeOH**. Upon heating, **2·MeOH** melted at 61–62 °C, which is near the boiling point of methanol, recrystallized at 71 °C, and finally melted at 94 °C, the same temperature as **2- α** . The single crystals of the two polymorphs of **3**, namely **3- α** and **3- β** , were obtained through the concentration of the reaction mixture and by recrystallization from ethanol, respectively. Each sample was composed of yellow needles with various thickness, which we could not judge as polymorphs with naked eyes. Through optical microscopy we observed that the major crystals of the as-prepared sample melted at 137 °C, while fine needles of the latter sample exhibited solid-to-solid phase transition at 131–135 °C, and then melted at 137 °C along with thicker needles. These observations cannot rule out the possibility that the both samples are a mixture of **3- α** and **3- β** phases. As discussed later, the powder XRD pattern of the as-prepared sample was fairly reproduced from the single crystal structure of **3- β** (m.p. 137 °C), and therefore we concluded that the metastable **3- α** (m.p. 131 °C) was a crystallographic impurity included in the as-prepared sample.

For thermal analyses (see the section below), we used the **1- α** , **2- α** , **3- β** samples as the initial states. In spite of our attempts to pick up crystal chips from the aluminum sample pans that underwent appropriate heating/cooling history in the DSC apparatus, the crystal structures of the other phases were not clarified. The crystal data, together with other relevant information regarding the structural determination, are listed in Table S4.

3.2 Phase Assignment by Simultaneous XRD-DSC. First, the thermal behavior of the as-prepared crystalline samples **1- α** , **2- α** , and **3- β** were examined by DSC (for more details see the Supporting Information). These samples exhibited totally different behavior from each other, especially during cooling/heating processes after their melting: **1** recrystallized in the cooling process (Figure S1); **2** remained in liquid or glass state without crystallization (Figure S2); **3** exhibited supercooling and subsequent cold crystallization (Figure S3). Because our present interest is in examining potential heat storage materials, we hereafter focus on the comparison between the phase transition behavior of **1** and **3**.

Figure 2 shows the XRD-DSC results for **1**, along with a powder X-ray diffraction (PXRD) pattern calculated from the single crystal data of **1- α** . The PXRD patterns i–iv, before melting at 118.7 °C, are almost identical to the calculated pattern of **1- α** . During the cooling process, the DSC curve showed an exothermic anomaly at 86.6 °C, from which the PXRD patterns (xi–xiii) showed different peaks from that of **1- α** . These patterns were also different from the patterns calculated for the **1- β** crystal, so we tentatively denote this recrystallized phase as **1- γ** , although its crystal structure is still unknown. After cooling to -10 °C, the sample was reheated. The **1- γ** crystal melted at 115.2 °C, and thereafter the DSC curves showed essentially iterative profiles.

Figure 3 shows the XRD-DSC results for **3**, along with PXRD patterns calculated for **3- α** and **3- β** . The initial state was identified as **3- β** , based on the comparison of its PXRD pattern (i) with the calculated patterns. Although there were only slight differences between the patterns of **3- α** and **3- β** , they are discriminable from the weak reflections at 11 and 14° of 2 θ . The sample was heated above its melting point (137.6 °C), and then cooled to -20 °C to be supercooled, showing a glass transition around -1 °C on the DSC curve. During the subsequent heating process, the PXRD patterns of the glass (below -5 °C, pattern ii) and supercooled liquid (up to 40 °C, pattern iii) both showed a halo corresponding to amorphous structure. Upon further heating, an exothermic anomaly was observed at 42.6 °C (T_{cc} -1), and simultaneously a set of sharp peaks emerged in the XRD pattern (iv–vi), which clearly demonstrates cold crystallization. The reflection peaks of the first cold crystal were not consistent with **3- α** or **3- β** . We tentatively denote this crystalline phase as **3- γ** , although its crystal structure is still unknown. Upon further heating, at approximately 85 °C (T_{cc} -2), the sample underwent solid-solid transformation to another crystalline phase (pattern vii), showing an exothermic anomaly with a broad peak over 70–100 °C. During this transformation, changes including the weakening of a peak at 6°, and unification of two peaks around 15–16° occurred. The PXRD patterns (viii–xii) were substantially unchanged until the sample was cooled to 25 °C after being raised to 125 °C at the maximum processing temperature. The PXRD pattern of the obtained crystal was

identical to the pattern calculated for **3- α** . It is worth noting that the cold crystal showed double melting peaks around 132 and 136 °C (as peak top temperatures). By careful inspection of the XRD-DSC results with a scan rate of 1 °C min⁻¹ (Figure S4), we found that the sample underwent another solid-solid transformation at around 131–135 °C to form **3- β** , which finally melted at 137 °C.

3.3 Solid-state UV-Vis spectroscopic analysis. The UV-Vis absorption spectra of the initial crystals are shown in Figure 4. The UV-Vis spectra of both **1** and **3** gave peaks at around 380, 410, 440, and 470 nm, whereas that of **2** had peaks at about 450 and 490 nm, with weak shoulder-peaks in the short wavelength region between approximately 380 and 430 nm. This difference in the absorption profile suggests a difference in the tautomer ratio since the peaks around 380–420 nm arise from the OH-form, while the peaks between 420–500 nm can be attributed to the NH-form. The small table inserted in Figure 4 shows the values of A_{sw} , the ratio of the short-wavelength components (defined in the experimental section), which can be a measure of the abundance of OH-form to the total amount of the tautomers.

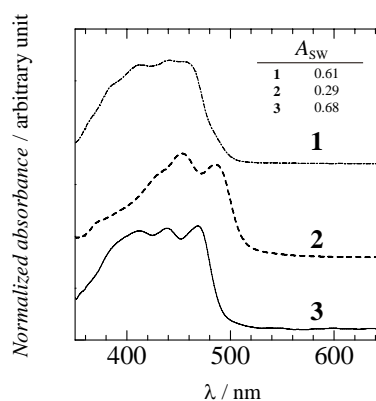


Figure 4. Result of UV-Vis spectra in 350–650 nm region in the initial crystals for **1** (**1- α**), **2** (**2- α**) and **3** (**3- β**) compounds.

Similarly, we measured the solid-state UV-Vis absorption spectra of the samples using a temperature-controlled stage placed across the optical path of the microscope. The temperature was changed at the same scanning speed as that of DSC (15 °C min⁻¹). The spectra of **1** and **3** at various temperatures are shown in Figures 5 and 6, respectively. The melting (T_m), crystallization (T_c) and cold crystallization (T_{cc}) temperatures were indicated with arrows, while the glass transition temperature (T_g) was indicated at the temperature determined by the DSC measurement.

In the first heating process of compound **1**, a slight decrease of the shoulder at 380 nm was observed when the temperature was increased from 25 to 50 °C. Upon further heating to the T_m (approximately 118 °C), another shoulder arose at 490 nm. After fusion, the shoulder rapidly grew to give a sharp onset at approximately 510 nm. During the subsequent cooling process, the spectrum gradually became fine-structured. After recrystallization, the peaks in the long wavelength region (450–490 nm) were remarkable. During the second heating process, the short wavelength region (370–450 nm) gradually increased. In contrast to the first heating process, the spectrum showed no change during fusion.

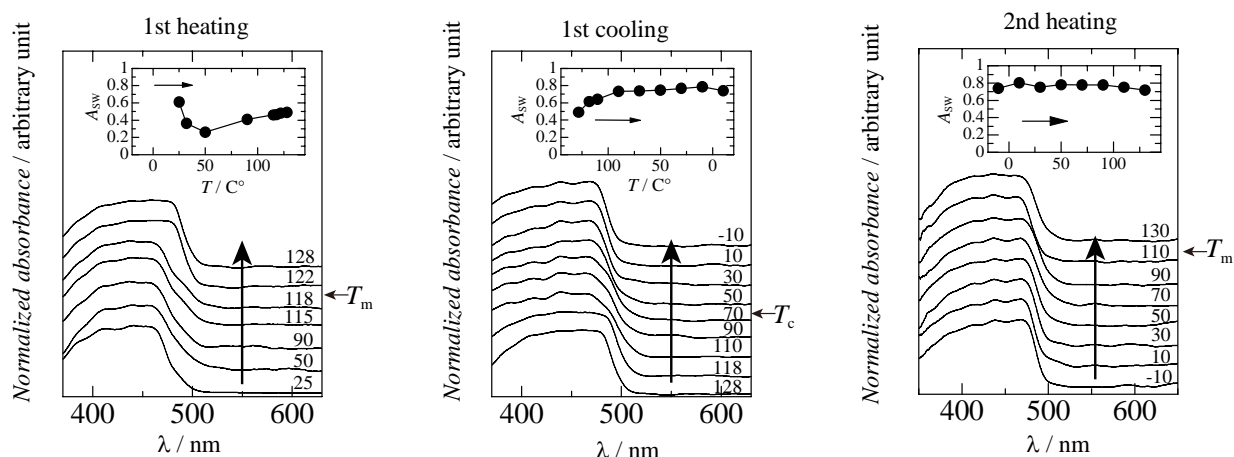


Figure 5. Temperature-dependent UV-Vis spectra in 350-650 nm region in first heating - cooling process and second heating process for **1** compound. T_m , melting; T_g , glass transition; T_c , crystallization; T_{cc} , cold crystallization.

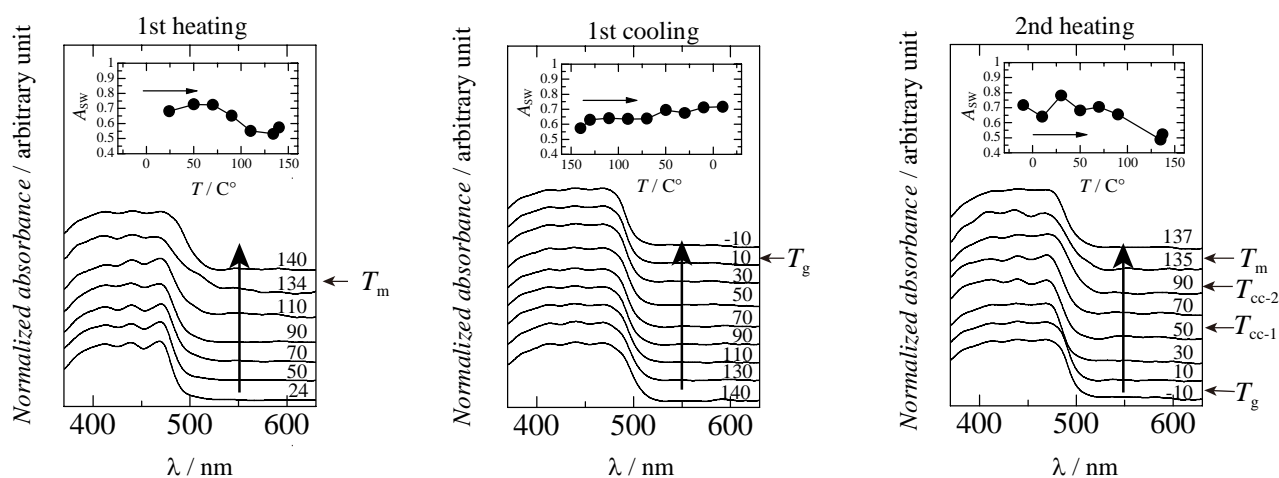


Figure 6. Temperature-dependent UV-Vis spectra in 350-650 nm region in first heating - cooling process and second heating process for **3** compound. T_m , melting; T_g , glass transition; T_c , crystallization; T_{cc} , cold crystallization.

For compound **3**, the spectrum did not change until approximately 70 °C in the first heating process. We observed the growth of a shoulder peak at approximately 490 nm prior to fusion. During the subsequent cooling process, the spectrum was almost unchanged, while the sample underwent supercooling and transformed into a glassy state. During the second heating process, the onset at the long-wavelength edge moderated after the glass transition temperature (~ 30 °C), and immediately the spectrum sharpened upon cold crystallization at T_{cc-1} . The spectrum became slightly broader with intensification of the shoulder peak at approximately 490 nm, while the second cold crystallization was observed at T_{cc-2} . After melting of the cold crystal, the spectrum became less-structured, and the shoulder at the long-wavelength edge disappeared. The insets in Figures 5 and 6 show the A_{5w} values.

4. Discussion

4.1 Relationship between UV-Vis absorption and tautomerism. The *o*-hydroxy aryl aldehyde Schiff bases are known to show thermochromism, originating from a temperature-dependent change in the relative abundance of the prototropic tautomers, i.e. the OH- and NH-forms. The thermochromic behavior changes depending on the relative stability of the tautomers, which may be influenced by π -electron delocalization, intramolecular hydrogen bonding, substituent effects, and temperature.³¹⁾ The three toluidine

derivatives used in this study were only differed with the position of their methyl group, which may be responsible for the observed differences in the thermal behavior and crystal structures. The UV-Vis absorption spectra of the initial crystals (**1- α** , **2- α** , and **3- β**) were noticeably different from each other, indicating a difference in the tautomer ratio of the Schiff bases.^{21,22)} However, the spectra of these Schiff base samples varied in a complicated fashion depending on the temperature and thermal history, suggesting that the spectral profile is not solely determined by the tautomer ratio. Some intermolecular interactions may influence the electronic transition, while other minor factors including π -conjugation effect is similar among these compounds. It may be expected that a precise peak decomposition analysis could reveal the relative abundance of the tautomers. Regrettably, each spectrum is considerably broad and fused so the unique solution of the peak decomposition could not be achieved. Therefore, we confined the number of the peak components to five, and introduced a parameter, A_{5w} , to characterize the spectral profiles (see the Experimental section). According to reported studies on the tautomerism of Schiff bases, the NH-form gives an absorption band in the longer wavelength region compared to the OH-form. Based on this conventional view, in this study, we tentatively regard this parameter as a measure of the abundance of the OH-form relative to all the tautomers present in the solid.

4.2 Potential surfaces of tautomers with respect to

phenyl rotation. In previous studies, the authors highlighted features observed for the potential surface of materials that exhibit cold crystallization. For example, the potential surfaces calculated

for bis[1-(toluyliminomethyl)naphthalene-2-olato]nickel(II)s had flat-bottomed regions around the energy minima with respect to the rotation of the phenyl groups.¹⁷⁻¹⁹ This suggests that the phenyl groups can rotate without noticeable energy change, indicating that the molecules have high conformational flexibility. Such flexibility prevents molecules from falling into a conformation appropriate for crystallization upon cooling, resulting in supercooling. Based on this assumption, we attempted to explain the thermal behavior of compounds **1** and **3**. In particular, compound **1** recrystallized upon cooling, whereas **3** showed no anomalies relevant to crystallization in the cooling process, and finally underwent a glass transition. We hypothesized that the potential surface of **3** has a shallow well around an energy minimum. To quantify this effect, we conducted quantum chemical calculations of the potential surfaces of the OH- and NH-forms, by varying the twist angle of phenyl group (ϕ_1 , Figure 1-(a)). The geometric data of the molecules were obtained by full optimization using from their crystal structures (**1- α** and **3- β**) as initial data. All calculations were performed at the level of B3LYP/6-311G** using the Gaussian09 program package³². Hereafter, we denote the calculated structures of the ideal OH- and NH-forms of **1**, as **1_{OH}** and **1_{NH}**, respectively, to discriminate from their observed forms. The potential surface of **1_{OH}** (Figure 7(A)) has two minima located at 150 and 210°, while that of **1_{NH}** (Figure 7(B)) has one shallow well spreading from 150 to 210°. This difference may be ascribed to the π -electron delocalization and intramolecular hydrogen bonding. At the angle of 180°, a bending structure of the N-phenyl group appears to contribute to stabilization, compensating the steric repulsion between the -OH and methyl groups. For both **1_{OH}** and **1_{NH}**, the obvious energy increase at $\phi_1 < 90^\circ$ and $270^\circ < \phi_1$ regions resulted from the steric repulsion between the methyl group and the azomethine and 8-naphthyl protons. In contrast, the potential surface of **3_{OH}** (Figure 7(C)) has four minima at 30, 150, 210, and 330°, owing to the rotational symmetry of the *p*-toluyl group. Similarly, the potential surface of **3_{NH}** (Figure 7(D)) has two shallow wells at approximately 0 and 180°.

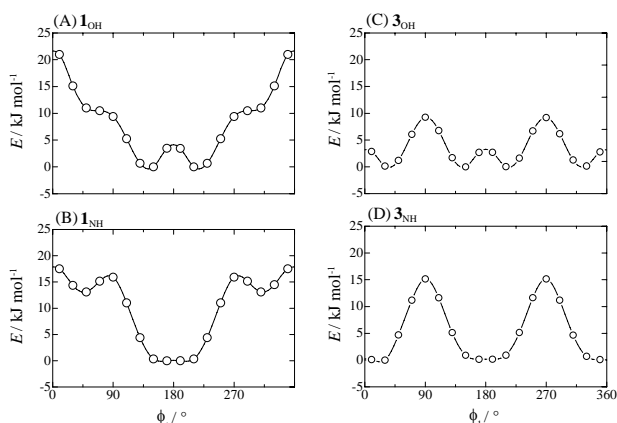


Figure 7. Difference in molecular energy of **1** and **3** in OH-form and NH-form between the fully optimized structure and that with varying ϕ_1 . (A), **1_{OH}**; (B), **1_{NH}**; (C), **3_{OH}**; (D), **3_{NH}**.

The calculated energy at the potential bottom of the OH-form was lower than that of the NH-form by 2.1 kJ mol⁻¹ for **1** and by 3.0 kJ mol⁻¹ for **3**. These energy differences are comparable to RT at ambient temperature ($\sim 25^\circ\text{C}$), suggesting

that the OH- and NH-forms are in equilibrium in the temperature range of the present study. Furthermore, because the flat-bottomed minima lead to a large density of states, the ratio of the NH-form increases rapidly as the temperature increases if the phenyl ring freely rotates or is liberated. Thus, it is suggested that the NH-form is present as a mixture of various rotamers in the molten state. On the other hand, during the cooling process, the OH-form easily falls into the energy-minimum structure, which is suitable for crystal packing along the relatively steep well, whereas the molecules in NH-form stay as a mixture of several rotamers. Based on these computational results, we can postulate the mechanism of supercooling for salicylideneaniline derivatives as follows: (1) at ambient temperatures, the tautomerization equilibrium is biased towards the OH-form; (2) as the temperature rises, the proportion of the NH-form increases; (3) in the molten state, the structural variety (torsion angle of phenyl ring) of the NH-form increases; (4) during the cooling process, some molecules in the OH-form begin to crystallize, while those in the NH-form interfere with the crystallization process. Salicylideneanilines are regarded as a “pure compounds” the crystalline state, but can actually be a mixture of different compounds in the molten state. If the proportion of the OH-form becomes sufficiently large for crystallization before the temperature reaches T_g , the melt of the compound crystallizes but otherwise gets supercooled.

4.3 The influence of tautomerism on cold crystallization.

The DFT results described above suggest that the molecules in the OH-form crystallize more easily than those in the NH-form. The variation in A_{SW} values estimated for the initial crystals (Figure 4) indicate that the optimal distribution of the tautomers depends on the crystal packing structure. These findings suggest that the crystallization would proceed more efficiently if the ratio of the tautomers is closer to an optimal value for crystallization. Following this hypothesis, we hereafter give a comprehensive explanation for the cold crystallization of **3**.

During the first heating process of **1- α** (Figure 5, left), the A_{SW} value rapidly decreased from 0.6 to 0.2 at 50 °C, and then exhibited a mild recovery to 0.5 when approaching the melting temperature. This change corresponds to the equilibrium shift upon temperature increase, and the latter change suggests the stabilization of the OH-form accompanied by alteration of the potential curve. In the subsequent cooling process, A_{SW} value increased to 0.7 at 70 °C, where sample crystallized to **1- γ** , and thereafter remained relatively constant. This coincidence of crystallization and saturation point of A_{SW} is consistent with our hypothesis. During the second heating process, the A_{SW} value remained almost constant along with the overall spectral profile until the sample melted. The spectral insensitiveness of the **1- γ** crystal to changes in temperature suggests an overwhelming stability of the OH-form in this crystal packing environment. Namely, the **1- γ** crystal is primarily a non-thermochromic phase, in contrast to the **1- α** crystal.

As for the **3- β** crystal in heating process, the A_{SW} value decreased from 0.7 to 0.5 when the temperature was increased from 70 °C to the melting point. Upon cooling, the A_{SW} value suggested relatively a high proportion of the NH-form in the temperature range from 140 to 50 °C, and gradually recovered to 0.7 by -10°C . This distribution of tautomers may have prevented the molecules from crystallizing due to the structural diversity with respect to the phenyl ring rotation, as suggested from the potential curve (Figure 7(C) and (D)). Upon further cooling, even though the A_{SW} value recovered to the level sufficient for crystallization, the sample did not allow for the nucleation and growth processes^{33,34} due to the rise of its viscosity, leading to vitrification. During the second heating

process, the absorption spectrum irregularly changed. The A_{SW} value showed a sudden increase between 50–70 °C (T_{cc-1}), and thereafter followed the trajectory similar to that of the first heating process until melting. Along this temperature course, we observed crystallization around 30 °C and solid-to-solid transition between 90–130 °C (T_{cc-2}) by microscopic analysis. These events were identified as a two-step cold crystallization process with thermal anomalies at 43 and 72 °C that were observed in the XRD-DSC results for **3** (Figure 3). The discrepancies in temperature between the two methods may have arisen from a difference in experimental conditions. For example, the thermal conductivity of the sample container varies between the glass for the microscope and Al for the DSC analysis. Therefore, we assigned the sharp increase of A_{SW} to the formation of the **3- γ** phase, and the following gentle decrease to the equilibrium shift of the tautomers in the **3- α** phase. Because the **3- β** phase appears over a narrow temperature range (135–137 °C), it is difficult to detect the change in the A_{SW} value transitioning from **3- α** to **3- β** . After the melt of the **3- β** phase, the A_{SW} remains at a relatively low value (0.5–0.6), suggesting that the NH-form-biased distribution is probable in the molten state, even if the liquid is supercooled.

The above considerations validate our hypothesis that the crystallization of the Schiff base samples is influenced by the balance between the distribution of the tautomers and the viscosity of their supercooled liquid state. The melt sample undergoes crystallization in the cooling process if the OH-form ratio reaches an appropriate value before the viscosity interferes with the crystallization. In contrast, the melt sample forms a supercooled glass if the OH-form ratio remains at a low level until the viscosity suppresses the nucleation and subsequent crystal growth. Even for the supercooled sample, cold crystallization occurs if the molecules recover sufficient mobility and appropriate tautomer ratio as the temperature rises.

5. Conclusion

In this study, we compared thermal behavior of three 2-hydroxy-1-naphthaldehyde Schiff base compounds derived from *o*-, *m*-, and *p*-toluidines by a series of simultaneous XRD-DSC measurements. We found that the subtle difference in molecular structure provided the compounds with remarkable changes in their crystal structure and phase transition behavior. Only the *p*-toluidine derivative exhibited supercooling followed by cold crystallization, while the *o*-isomer showed ordinary melting-crystallization cycles, and the *m*-isomer showed irreversible vitrification. These Schiff base compounds showed distinct absorption spectra, depending on the distribution of their prototropic tautomers, i.e. the OH- and NH-forms. DFT calculations suggested that the NH-form has a flat-bottomed potential well depending on phenyl rotation, which prevents the molecule from rapidly crystallizing. The solid-state, variable-temperature absorption spectra enabled the discussion of changes in the distribution of the tautomers along with the phase transition behavior. The results were consistent with our hypothesis that the rate of crystallization is influenced by the ratio of the tautomers and viscosity of the sample. Specifically, the melt sample forms a supercooled glass if the OH-form ratio remains low until the viscosity suppresses the nucleation and subsequent crystal growth. This hypothesis gives a reasonable explanation for the cold crystallization of the supercooled samples. Considering structural demand for developing cold crystallization, it is notable that compound **3** satisfied the two guidelines proposed in previous studies:¹⁷⁻¹⁹⁾ 1) nearly-free rotation of the phenyl ring increases the degree of freedom of molecular motion, and 2) coexistence of OH/NH tautomers interconvertible in the liquid (molten) state disturbs

the homogeneity of the system.

Supplementary Material

DSC charts for analyses of phase relation of **1- α** , **2- α** and **3- β** , XRD-DSC chart of cold crystal (**3**) obtained in the heating processes at 125.0–139.6 °C (scan rate: 1 °C min⁻¹) compared with simulated pattern based on crystal structures (**3- α** and **3- β**) determined independently. An example of the resolution of a UV-Vis spectrum into five gaussians through a curve fit. Atomic coordinates of fully optimized **1** and **3** molecules in vacuum.

Acknowledgement

The authors are grateful to professor emeritus Hiroshi Nakamura for his helpful instruction of Marquardt method and distribution of the home-made program.

A part of this work was conducted at Advanced Characterization Nanotechnology Platform of the University of Tokyo, supported by "Nanotechnology Platform" of the Ministry of Education, Culture, Sports, Science and Technology (MEXT), Japan.

References

- V.V. Tyagia, S.C. Kaushika, S.K. Tyagib, T. Akiyamac, *Renew Sustain Energy Rev.* **2011**, *15*, 1373-1391.
- K. Manjunath, C. S. Kaushik, *Renewable & Sustainable Energy Reviews* **2014**, *40*, 348.
- H. Ogura, T. Yamamoto, H. Kage, *Energy* **2003**, *28*, 1479-1493.
- D. Mileva, I. Kolesov, R. Androsch, *Colloid Polym Sci* **2012**, *290*, 971-978.
- M. Di Lorenzo, M. Gazzano, M. Righetti, *Macromolecules* **2012**, *45*, 5684-5691.
- H. Tsuji, L. Bouapao, *Polym Int* **2012**, *61*, 442-450.
- T. Endo, T. Kato, K. Tozaki, K. Nishikawa, *J. Phys. Chem. B* **2010**, *114*, 407-411.
- K. Piela, I. Turowska-Tyrk, M. Drozd, M. M. Szostak, *J. Mol. Struct.* **2011**, *991*, 42-49.
- S. Sampath, A. A. Boopathi, A. B. Mandal, *Phys. Chem. Chem. Phys.* **2016**, *18* (31), 21251-21258.
- A. Honda, Y. Takahashi, Y. Tamaki, K. Miyamura, *Chemistry Letters* **2016**, *45* (2), 211-213.
- S.-J. Kim, T. E. Karis, *J. Mater. Res.* **1995**, *10*(8), 2128-2136.
- Q. Wang, A. Takeuchi, Y. Yamamura, K. Saito, W. Mori, M. Sorai, *J. Phys. Chem. B* **2008**, *112*, 11039-11048.
- N. Arai, M. Sorai, S. Seki, *Bull. Chem. Soc. Jpn.* **1972**, *45*(8), 2398-2406.
- Z. Rezvani, A. R. Abbasi, K. Nejati; M. Seyedahmadian, *Polyhedron* **2005**, *24*, 1461-1470.
- Y. Shirota, *J. Mater. Chem.* **2000**, *10*, 1-25.
- S. P. Das, R. Ganguly, Y. Li, H. S. Soo, *Dalton Transactions* **2016**, *45* (34), 13556-13564.
- K. Iwase, H. Houjou, Y. Yamamura, K. Saito, *Chem. Lett.* **2013**, *42*, 1040-1042.
- K. Iwase, Y. Nagano, I. Yoshikawa, H. Houjou, Y. Yamamura, K. Saito, *J. Phys. Chem. C* **2014**, *118*, 27664-27671.
- K. Iwase, I. Yoshikawa, H. Houjou, Y. Yamamura, K. Saito, *Bull. Chem. Soc. Jpn.* **2015**, *88*, 989-995.
- H. Achira, I. Yoshikawa, H. Houjou, *Chem. Lett.* **2016**, *45*(12), 1415-1417.
- K. Amimoto, T. Kawato, *J. Photochem. Photobiol. C: Photochemistry Reviews* **2005**, *6*(4), 207-226.
- E. Hadjoudis, I. M. Mavridis, *Chem. Soc. Rev.* **2004**, *33*, 579-588.

23. H. Joshi, F. S. Kamounah, G. van der Zwan, C. Gooijera, L. Antonov, *J. Chem. Soc., Perkin Trans. 2* **2001**, 2303-2308.
24. S. R. Salman, J. C. Lindon, R. D. Farrant, T. A. Carpenter, *Magn. Reson. Chem.* **1993**, *31*, 991-994.
25. G. M. Sheldrick, *Acta Crystallogr.* **2008**, *A64*, 112-122.
26. M. C. Burla, R. Caliandro, M. Camalli, B. Carrozzini, G. L. Casciarano, L. D. Caro, C. Giacovazzo, G. Polidori, D. Siliqi & R. Spagna, *J. Appl. Cryst.* **2007**, *40*, 609-613.
27. D. W. Marquardt, *J. Soc. Indust. Appl. Math.* **1963**, *11*, 431-441.
28. R. Tahara, T. Morozumi, H. Nakamura, *J. Phys. Chem. B* **1997**, *101*, 7736-7743.
29. B. Kaitner, E. Meštrović, G. Pavlović, *J. Chem. Crystallogr.* **1998**, *28*, 77-82.
30. A. K. Baghdouche, S. Mosbah, Y. Belhocine, L. Bencharif, *Acta Cryst.* **2014**, *E70*, o676.
31. T. M. Krygowski, H. Szatyłowicz, O. A. Stasyuk, J. Dominikowska, M. Palusiak, *Chem. Rev.* **2014**, *114*, 6383-6422.
32. M. J. Frisch, G. W. Trucks, H. B. Schlegel, G. E. Scuseria, M. A. Robb, J. R. Cheeseman, G. Scalmani, V. Barone, G. A. Petersson, H. Nakatsuji, X. Li, M. Caricato, A. Marenich, J. Bloino, B. G. Janesko, R. Gomperts, B. Mennucci, H. P. Hratchian, J. V. Ortiz, A. F. Izmaylov, J. L. Sonnenberg, D. Williams-Young, F. Ding, F. Lipparini, F. Egidi, J. Goings, B. Peng, A. Petrone, T. Henderson, D. Ranasinghe, V. G. Zakrzewski, J. Gao, N. Rega, G. Zheng, W. Liang, M. Hada, M. Ehara, K. Toyota, R. Fukuda, J. Hasegawa, M. Ishida, T. Nakajima, Y. Honda, O. Kitao, H. Nakai, T. Vreven, K. Throssell, J. A. Montgomery, Jr., J. E. Peralta, F. Ogliaro, M. Bearpark, J. J. Heyd, E. Brothers, K. N. Kudin, V. N. Staroverov, T. Keith, R. Kobayashi, J. Normand, K. Raghavachari, A. Rendell, J. C. Burant, S. S. Iyengar, J. Tomasi, M. Cossi, J. M. Millam, M. Klene, C. Adamo, R. Cammi, J. W. Ochterski, R. L. Martin, K. Morokuma, O. Farkas, J. B. Foresman, and D. J. Fox, Gaussian 09, Revision D.01, D. J. Gaussian, Inc., Wallingford CT, **2009**.
33. R. Boistelle, J. P. Astier, *J. Cryst. Growth* **1988**, *90*, 14-30.
34. D. Turnbull, *J. Appl. Phys.* **1950**, *21*, 1022-1027.